MECHANICS OF MATERIALS

Effects of thermal gradient and residual stresses on thermal barrier coating fracture

G. Qian [a], T. Nakamura [a,*], C.C. Berndt [b]

[a] *Department of Mechanical Engineering, State University of New York, Stony Brook, NY 11794, USA*
[b] *Department of Materials Science and Engineering, State University of New York, Stony Brook, NY 11794, USA*

Abstract

Driving mechanisms which lead to internal crack growth and failure in the thermally sprayed coatings are identified using detailed finite element models. Coatings are assumed to contain embedded cracks and they are thermally loaded according to a typical high temperature environment. In order to determine the accurate stress state, the thermal gradient within the coating is calculated from the steady-state heat transfer analysis. Our models take into account various locations of cracks, temperature-dependent and -independent plasticity, thermal conductivities of different layers and thermal insulation across crack surfaces. The results indicate that the energy release rate of large cracks can reach close to fracture toughness of ceramic coatings. We have also studied the effect of residual stresses on the fracture behavior. For a penny-shaped crack located parallel to the coating layers, a limited influence of residual stresses is observed. The effect is more pronounced when the crack orientation is perpendicular to the coating layers where it has shown a beneficial influence. In both cases, the effects of residual stresses are relevant to the cracks close to the ceramic–bond interface. In addition, we have modeled functionally graded material and investigated its mechanical influence on the embedded cracks. The implications of the present work to internal crack initiation and growth, which can lead to coating failure, are also addressed. © 1998 Elsevier Science Ltd.

1. Introduction

Thermal barrier coatings (TBCs) sprayed onto a substrate provide high temperature protection to machine parts and improve their efficiency. In recent years, industrial applications of various TBCs have increased significantly (Liebert and Miller, 1984; Miller, 1997). One of more common fabrication techniques is plasma spray processing where ceramic powder is melted and sprayed onto a substrate. This process renders a unique microstructure consisting of voids and defects within a porous coating microstructure. Moreover, many coating material properties differ from those of the corresponding bulk materials. For example, the elastic modulus of zirconia-based coatings is only about one fourth of that of bulk zirconia (Herman and Shankar, 1987; McPherson, 1989; Bengtsson and Johannesson, 1995).

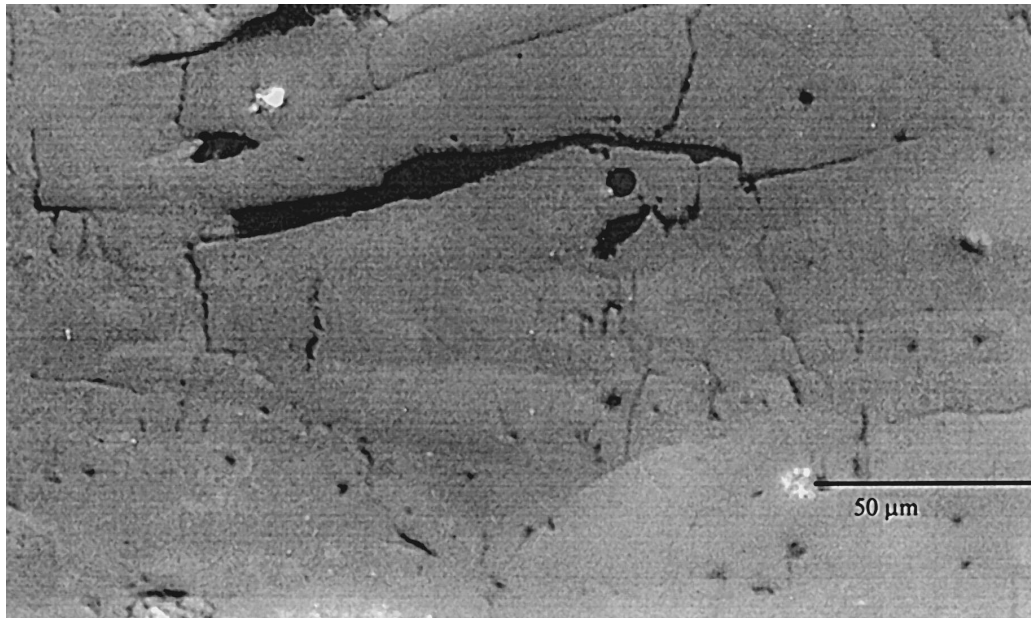* Corresponding author. E-mail: nakamura@plast.eng.sunysb.edu.

Fig. 1. Micrograph showing cross-section of plasma-sprayed alumina–titania (Al_2O_3–TiO_2) A relatively large flaw parallel to the coating layer can be seen.

The adhesion between the as-sprayed ceramic and substrate metal is usually not very strong. Therefore, some material (usually metallic) which has high affinities to both the ceramic and substrate materials is chosen and sprayed onto the substrate before overlaying the ceramic coating. The intermediate metallic coating is called a bond coat. Since TBCs consist of thin layers of materials with different mechanical and thermal properties, there arises significant boundary layer effects. The TBCs also exhibit a porous microstructure and this effect interacts with internal voids and flaws and may cause them to develop into relatively large cracks. The micrograph shown in Fig. 1 depicts the cross-section of thermally sprayed coating containing voids and cracks. These internal cavities may generate stress concentration and grow to large-sized cracks under thermal loading conditions. Thus, the fracture behavior of coatings due to their microstructural defects are important in formulating a comprehensive understanding of the toughness of TBCs (Bartlett and Maschio, 1995).

In this paper, various conditions which affect fracture behavior are investigated towards minimiz-
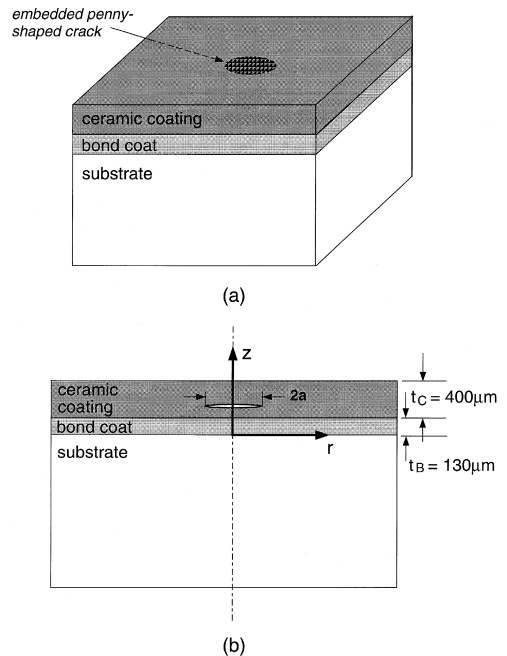

Fig. 2. (a) Schematic of embedded penny-shaped crack in the thermal barrier coating model consisting of the ceramic and bond coatings and the substrate. (b) Cross-sectional view of axisymmetrical model.

ing the TBC failure due to internal crack growth. It is assumed that a penny-shaped crack exists within the coating system and the TBCs are exposed to a high temperature environment as shown in Fig. 2(a). The only loading arises from thermal stresses and no external load such as impact (e.g., from particulates in the fuel gas or other foreign objects) and vibrations is considered. Our aim is to present a wide range of the thermo-mechanical response and performance of the TBCs through detailed fracture analysis. In carrying out the simulation study, we have estimated the temperature field within the coatings by using steady-state heat transfer analysis. According to prescribed temperature boundary conditions, the temperature gradient through the coating thickness is determined from the thermal conductivities of ceramic and bond coatings. Furthermore, we have considered an insulation effect across an opened crack. This effect results in a temperature discontinuity across crack faces and a complex temperature distribution very near the crack tip. The thermal insulation of a crack was found to have a great impact on the fracture parameters (Hutchinson and Lu, 1995; Qian et al., 1997).

The residual stresses which are induced in the fabrication process of the TBCs are, a priori, associated with many mechanical failures of the coating. For example, delamination may occur along the interface of the pre-tensioned coatings (Kokini et al., 1997) while the compressive residual stress may cause spalling inside the coatings (Bartlett and Maschio, 1995). The mechanisms whereby residual stresses are generated within thermal spray coatings have been discussed extensively (Hobbs and Reiter, 1988; Elsing et al., 1990; Takeuchi et al., 1990). The residual stresses and their effects on the fracture parameters will be examined quantitatively in this paper. In order to gauge the effect of residual stresses on a crack with different orientation, additional calculations are also carried out for an embedded crack perpendicular to the coating layers.

In high temperature environments, the bond coat and substrate which are made of metallic materials may undergo elastic–plastic deformation. This necessitates modeling them as elastic–plastic materials for accurate determination of their nonlinear behavior. We have carried out the analysis by assuming the bond coat and substrate to be both temperature-dependent and temperature-independent elastic–plastic materials. The behavior of all coating materials is described in Section 2. Furthermore, we have modeled a functionally graded material (FGM) between the ceramic and bond coatings. The concept of FGMs has emerged as a hybrid material with prospects for many industries. A simple elastic–plastic model of a ceramic/metal mixture is also proposed to study the elastic–plastic response of TBCs containing a FGM layer.

2. Material model

The coating system considered here represents a typical ceramic–metal–metal configuration. For the ceramic surface coating, we have chosen $ZrO_2 + 6$ wt% Y_2O_3, which is often referred to as yttria-stabilized zirconia (YSZ). Although it can creep at a very high temperature, we have assumed YSZ to remain linearly elastic for the range of temperature considered ($< 1100°C$) and no temperature dependent effect is included throughout our analysis. In addition, YSZ is modeled as an isotropic material and the small anisotropy usually found in sprayed YSZ (Leigh, 1996) is ignored. The YSZ and NiCrAlY, which are chosen for the surface and bond coats, are substantially softer than corresponding bulk materials. Typically, a thermally sprayed TBC contains 10 to 20% volume fraction of voids and cracks. In one respect, they are required for the insulation effect but in another respect, the voids cause the coating to be mechanically soft and weak. The bond coat and substrate are usually made of metal-based materials and they can deform plastically before failure. The plastic flow or yielding of the bond coat and substrate directly affects the residual stresses and fracture parameters of TBCs, especially at high temperature, and they are essential in understanding the mechanical characteristics of TBCs under thermal loading. In this analysis, the bond coat is assumed to be plasma sprayed NiCrAlY while the substrate is modeled as bulk Ti–6Al–4V.

In this analysis, the YSZ surface coat and NiCrAlY bond coat are modelled as two distinct layers with a clearly-marked straight-line interface between them. But it should be noted that the trans-

Table 1
Temperature-independent material properties

Materials	YSZ	NiCrAlY	Ti–6Al–4V
E (GPa)	20	115	67
ν	0.25	0.25	0.30
σ_0 (MPa)	N/A	49	40
H (GPa)	N/A	5	5
α (μ/°C)	10.0	15.0	10.2
k (W/m·°C)	1.0	22.0	20.0

Note: NiCrAlY properties are taken at $T = 900$°C and Ti–6Al–4V properties are taken at $T = 700$°C, shown in Table 2.

port of oxygen through YSZ which causes the oxidation of some metal elements especially aluminum in the bond coat results in a distinct intermediate oxide layer principally made of Al_2O_3 between the YSZ and NiCrAlY layers (Lee et al., 1989). The relative thickness of this intermediate oxide layer is usually very small, e.g., Lee et al. (1989) have observed such thickness to be a few microns. From the mechanical point of view, a very thin layer should not affect the structural response of TBC although it may be an important factor as a possible fracture initiation site.

Since limited material data exist on NiCrAlY and Ti–6Al–4V at high temperature, we have made the following assumptions on their properties. First, both are modeled as linearly hardening materials after yielding. This idealization of stress-strain relation should not significantly affect the overall deformation of the TBCs. In the elastic–plastic analyses, the

following constitutive equations under uniaxial loading condition are assumed for both materials:

$$\epsilon = \begin{cases} \sigma/E & \text{for } \sigma < \sigma_0, \\ \sigma_0/E + (\sigma - \sigma_0)/H & \text{for } \sigma \geq \sigma_0. \end{cases} \quad (1)$$

Here E is the Young's modulus, σ_0 is the yield stress, and H is the tangent modulus in the plastic range for each material. The J_2 flow theory of plasticity is implemented for multidimensional conditions. For simplicity, we have not considered time-dependent effects (e.g., creep) here. In the current analysis, we have chosen two sets of material models, one *temperature-independent* and the other *temperature-dependent*. The temperature independent properties of the three materials are listed in Table 1. In the table, α is the coefficient of thermal expansion (CTE) and k the thermal conductivity of the materials. The temperature-dependent properties for the bond coat (NiCrAlY) and the substrate (Ti–6Al–4V) are shown in Table 2. These values are obtained from various sources (Siemers and Melan, 1983; McPherson, 1989; Brandon and Taylor, 1989; Brandes et al., 1992; Illavsky et al., 1993; Cook et al., 1994). Due to the lack of sufficient available data, the tangent moduli for the two materials are taken to be $H = 5$ GPa throughout the temperature range considered in this analysis. Similarly, the thermal conductivity of each material is also assumed to be temperature-independent. Such an assumption should not cause much inaccuracy as long as the ratio of thermal conductivities of YSZ and NiCrAlY

Table 2
Temperature-dependent material properties

NiCrAlY														
T (°C)	20	200[a]	300[a]	400[a]	500	600	750	800[a]	900	1000	1100			
E (GPa)	200	183	174	164	155	147	138	130	115	98	80			
σ_0 (MPa)	1150	1146	1144	1142	1140	915	270	196	49	32	16			
α (μ/°C)	13	13	13	13	13	13	13	14	15	15	15			
Ti–6Al–4V														
T (°C)	20	100	150	200	260	300	400	480	500	540	600	650	700	1000[a]
E (GPa)	106	102	99	96	93	90	85	78	79	77	73	70	67	50
σ_0 (MPa)	970	825	768	710	671	645	580	476	450	320	125	83	40	10
α (μ/°C)	9.8	9.8	9.8	9.8	9.9	9.9	9.9	10.0	10.0	10.1	10.2	10.2	10.2	10.2

[a] Values at this temperature are linearly intrapolated or extrapolated from the known values at other temperatures.
Note: ν, H and k are assumed to be independent of temperature and corresponding values in Table 1 are used.

remains nearly constant under various temperatures. We note that the temperature *independent* properties of NiCrAlY are taken at 900°C of Table 2. This temperature is close to the estimated temperatures of the bond coat when the surface of the ceramic coating is subjected to 1100°C. For the Ti–6Al–4V, we have chosen its properties at 700°C in Table 2. Although this temperature is somewhat lower than the imposed temperature for the substrate used in our model, it should be close to the through-thickness average temperature of actual thick substrate.

3. Stress and thermal fields within TBC

3.1. Fracture parameters

For the current analyses, a crack which exhibits the features of penny-shape is modeled as an embedded flaw in the TBCs as shown in Fig. 2. For simplicity, the horizontal dimensions of the coatings are chosen to be very large compared to the radius of the penny-shaped crack and the thicknesses of coating layers. Also no interactions with nearby cracks and/or voids are considered. Such a geometrical condition allows the stress and deformation near the crack to be axisymmetrical and costly three-dimensional analysis can be avoided. The axisymmetrical model offers an advantage over other 2D models, e.g., plane stress and plane strain, since there is no ambiguity of 3D effects. In addition, we assume the substrate to be thick so that the only characteristic geometrical lengths are the crack radius a and the thicknesses of the ceramic coat t_C and the bond coat t_B.

In order to characterize the crack driving force and toughness of cracks in layered or bimaterial structures under mixed-mode loading conditions, various studies have established that the energy release rate $\mathscr{G}$ and the phase angle ψ are the most suitable set of fracture parameters (Cao and Evans, 1989). When employing models based on either the linear fracture mechanics or the elastic–plastic fracture mechanics without crack growth or large elastic unloading, the energy release rate is equivalent to the path-independent J-integral. To facilitate the evaluation of $\mathscr{G}$ in the finite element analysis, the integral is represented in a domain integral form (Shih et al., 1986) as

$$\mathscr{G} = \frac{1}{a} \int_A \left\{ \left[\sigma_{\beta\gamma} u_{\beta,r} - W\delta_{r\gamma} \right] rq_{,\gamma} \right.$$
$$\left. + \left[\sigma_\theta u_{r,r} - W + \alpha\sigma_{kk}T_{,r}r \right] q \right\} \mathrm{d}A, \qquad (2)$$

where a is the crack radius, q is a weighting function which is a smooth function in the domain of integration. The mechanical strain energy is defined as

$$W = \int_A \sigma_{\beta\gamma} \, \mathrm{d}\epsilon_{\beta\gamma}^m, \quad \text{where } \epsilon_{\beta\gamma}^m = \epsilon_{\beta\gamma} - \alpha T\delta_{\beta\gamma}. \qquad (3)$$

Here T denotes the temperature change and the indices β, γ range over r, z. The above integral is specially formulated for the crack in axisymmetrical geometry and implemented in our post-processing code.

When a crack is embedded in a layered medium, the mismatch of the adjoining material properties generates shear deformation near the crack tip. This causes the so-called 'mixed-mode' fracture even under symmetrical loading conditions. Since the fracture resistance given in terms of $\mathscr{G}$ is strongly dependent upon the ratio of the mode I and II stress intensity factors, it is essential to evaluate the mixed-mode K_I and K_{II} of a crack in the layered medium. In general, most cracks show higher critical energy release rate when K_{II} is relatively larger than K_I. In order to extract the stress intensity factors, a computational approach involving an interaction energy integral is used for cracks in linearly elastic materials. The interaction energy release rate is based on the principle of superposition, and it can be used to numerically separate K_I and K_{II}. The domain integral formulation of the interaction energy release rate for the axisymmetric problems can be found in Nahta and Moran (1993) and Qian et al. (1997).

Once K_I and K_{II} are extracted from the finite element solutions, the nondimensional phase angle ψ is used to quantify the ratio of the shearing mode (mode II) to the opening mode (mode I). It is defined as

$$\psi = \tan^{-1} \frac{\mathrm{Im}(\mathbf{K}L^{i\epsilon})}{\mathrm{Re}(\mathbf{K}L^{i\epsilon})} \simeq \tan^{-1}\left(\frac{K_{II}}{K_I}\right) \qquad (4)$$

Here $\mathbf{K} = K_{\mathrm{I}} + iK_{\mathrm{II}}$ is called the complex stress intensity factor and L is a characteristic length. For a homogeneous crack, the above phase angle is independent of L, and it is equal to the right-hand expression of Eq. (4). When the crack is located within the elastic–plastic bond coat or along the interface between the ceramic and bond coats, the mixed-mode stress intensity factors can not be extracted from the interaction energy integral. In these cases the phase angle is determined from the stresses ahead of the crack as,

$$\psi = \tan^{-1}\left(\frac{\sigma_{rz}}{\sigma_z}\right) \quad \text{at } \theta = 0° \text{ and } r = L. \tag{5}$$

As in the case of Eq. (4), this phase angle depends on the characteristic length L. In order to establish a consistent definition of ψ, we have evaluated ψ for several different elastic interface cracks with various L. It was found that when $L = 2$ μm is chosen, ψ determined from Eqs. (4) and (5) yield similar values for these cracks. Based on this result, the phase angle obtained either by Eq. (4) or Eq. (5) throughout the paper is presented for $L = 2$ μm.

3.2. Steady-state heat transfer

3.2.1. Thermal gradient within TBC

In this study, a coupled steady-state temperature and stress analysis is carried out. We have assumed that the heating/cooling process is sufficiently slow so that the transient heat transfer conditions are not important. The influences from radiation and the 'edge' conduction are also ignored. In carrying out the analysis, we have assumed that the top surface of the ceramic coating is exposed to a uniform environment temperature. Within the ceramic and bond coats, the temperature decreases with depth until the boundary between the bond coat and the substrate is reached. Since the thermal conductivity of the substrate is much higher than that of TBCs, the temperature field of the whole substrate is modeled to be constant. The temperature drop through the coating represents the insulation effect of the TBCs.

In a high temperature environment, the actual temperature distribution within the coating can be difficult to obtain due to its microstructure and unsteady boundary temperature. Instead of using a complex model to estimate the precise temperature drop across the TBC (i.e., the difference between surface and substrate temperatures), we have assumed it to vary linearly with the imposed surface temperature. Consequently, the prescribed temperatures at the surface and in the substrate are increased linearly from room temperature (20°C) but at different rates. Initially, when there are no stresses in the TBCs, the temperature of whole model is set at 20°C. Then, the surface temperature T_{surf}, i.e., the temperature on the top surface of the ceramic, is gradually increased to the maximum temperature of 1100°C while the substrate temperature T_{sub} is increased to 850°C. Thus, this thermal condition assumes the insulation or the temperature drop of $\Delta T = 250°C$ across the coating at the last thermal load step. Alternately, the temperature difference between the surface and the substrate is less than 250°C during the loading. The temperature distribution within the coatings during the loading is determined from the finite element calculations. When no crack exists in the TBCs, such a boundary condition will give a simple one-dimensional temperature variation through the thickness. However, when the insulation effect across crack faces is considered, the temperature field becomes more complex, especially near the crack tip (see Section 3.2.2), and must be determined numerically. The thermal conductivities of the ceramic and the bond coats are shown in Table 1. Since the bond coat material is much more thermally conductive than that of sprayed YSZ, most of the temperature drop within the TBC occurs across the ceramic coating layer.

3.2.2. Insulation effect across crack faces

In the present analysis, another type of conduction mechanism is considered. When a relatively large crack (compared to voids and microcracks) opens up, trapped air between the crack faces acts as a thermal 'shield' against the otherwise normal heat flow through thickness because of its low thermal conductivity. In fact, the thermal conductivity of dry air is only about 0.07 W/m · °C at 900°C (Touloukian, 1970). This de facto thermal insulation by a crack results in the large temperature jump across the crack faces and promotes higher stress concentration. Such an effect was studied by Hutchinson and Lu (1995)

who have shown that a discontinuous temperature field across the crack faces in a ceramic coating can significantly increase the energy release rate. Essentially, the temperature jump over the crack enhances the thermal expansion difference in the regions above and below the crack and generates a large mode II or shear loading near the crack tip. Subsequently, the insulation across the crack faces may promote crack extension through increased crack driving force.

The temperature jump across the crack faces are mainly controlled by the heat conductance h_C over the crack (Eckert and Drake, 1972; Hutchinson and Lu, 1995). A large h_C indicates less thermal insulation and small temperature jump across the crack faces. In our analysis, we have chosen the heat conductance h_C over opened crack faces to be a linear function of the crack opening displacement δ as,

$$h_C = 1 \times 10^4 \text{ W/m}^2 \cdot {}^\circ\text{C}$$
$$- (5 \times 10^8) \cdot \delta \text{ W/m}^2 \cdot {}^\circ\text{C}. \tag{6}$$

Here δ varies along the crack faces depending upon the local opening displacement. In general, h_C increases with the loading temperature.

To illustrate the temperature profile of the TBC with a crack, the near tip 3D temperature contours are shown in Fig. 3. This model corresponds to an elastic–plastic crack ($a = 2$ mm) in the ceramic layer ($d = 0.4$ mm) to be analyzed in Section 5.2. The surface and substrate temperatures are prescribed as 1100°C and 850°C, respectively. The crack tip is
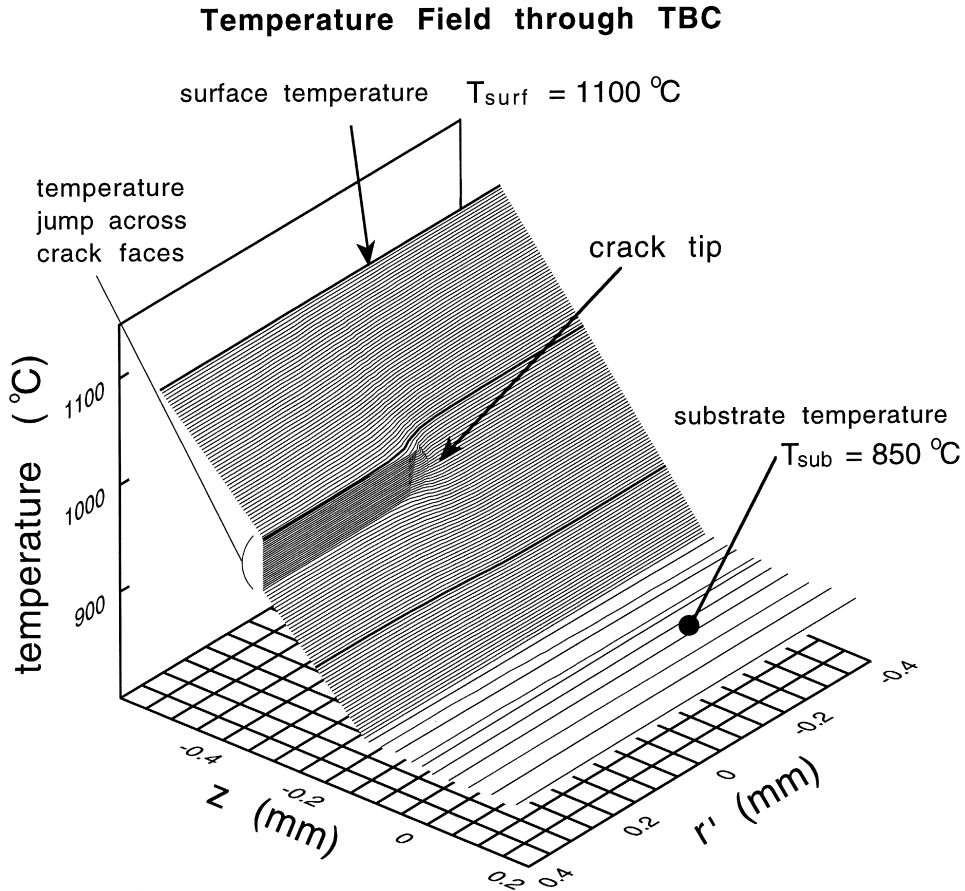

Fig. 3. Temperature field through thickness near the crack tip. The jump in the temperature occurs across the crack laces.

located at $z = 0.2$ mm and $r' = 0$ (note $r' = r - a$). It is clear that a sharp temperature jump across the crack faces exists and a complex temperature field around the crack tip can be observed. At large r' which is sufficiently ahead of the crack tip, the temperature variation is nearly linear with z. Moreover, most of the temperature drop occurs in the ceramic layer and a very small insulation effect is observed for the bond coat.

3.3. Residual stresses

Residual stresses are believed to affect the TBC integrity in high temperature applications. Brindley (1995) conducted some experiments showing that the thermal fatigue lifetime of some TBCs is directly related to the magnitude of the residual stresses. Many different mechanisms related to the residual stresses in TBCs have been discussed (Elsing et al., 1990; Takeuchi et al., 1990). Some of these mechanisms and their aftermath are addressed separately here.

The first mechanism concerns phase transformations. For example, unstabilized pure zirconia which cools down from an impinging temperature well above 2000°C to room temperature will transform from tetragonal phase to monoclinic phase. This phase transformation will bring about an internal volume increase of 8% inside the zirconia (Bever, 1986) and vice versa. Consequently, very large residual stresses will appear as a result. But in the real applications, pure zirconia is rarely used. Instead, the partially stabilized zirconia (PSZ), for example, $ZrO_2 + 6 \sim 8$ wt% Y_2O_3 where yttria is added as stabilizer, is used (Herman and Shankar, 1987). The added stabilizer can minimize the phase transformation effect and keep the highly disruptive volume change at bay. Therefore, residual stresses due to the phase transformation are neglected in this paper.

The second mechanism is the solidification process of the molten coating powder on top of its substrate after exiting from the nozzle of the spraying gun. The temperature of the molten powder is usually from $T_{exit} = 2500$°C to 3000°C (Harding et al., 1995). Since the cooling rate of the spraying particle is very high, typically about 10^6°C/s (McPherson, 1989), it takes only about 1 ms for the very thin splat (a few micrometers in thickness) to con-

tract and condense on the underlying material which is extremely thick relative to the splat. Therefore, the underlying substrate can be regarded as rigid compared to the impinging and condensing thin layer of splat. Consequently, the ensuing residual stresses in the condensing splats due to the solidification are tensile stresses. The magnitude of the tensile residual stress from the above scenario can be estimated from $\sigma = E_c \alpha_c (T_{exit} - T_{dep})$, where E_c and α_c are the modulus and CTE of the splat and T_{dep} is the deposition temperature (200 ∼ 400°C). According to such a formula, the stress can reach as high as 200 MPa. This estimation is purely theoretical. In practice, residual stresses due to the solidification are not significant since other ongoing processes reduce the tensile residual stresses. First, the tensile stresses inside coatings will inevitably induce microcracking and other structural degradation which in turn can reduce the tension inside the coatings. This process is similar to stress relaxation. On the other hand, the continual deposition of material on top of the previously deposited laminae of coating will induce compressive stresses underneath the current layer of deposition. As the thickness of coating builds up, much of the tensile residual stress induced during solidification might be compensated by the compressive stresses. All of these facts imply that the actual residual stress due to primary cooling is much smaller than that predicted theoretically. Some authors have argued that the solidification is quite insignificant in terms of generating the residual stresses in coatings (Takeuchi et al., 1990).

The third mechanism is secondary cooling where the coating system and substrate cool from the deposition temperature to room temperature. The mismatch of the CTEs of different materials is the major reason that large residual stresses ensue after cooling. This secondary cooling process is generally regarded as the prime mechanism related to the residual stresses which affect the overall integrity of the coatings.

4. Linear elastic model

4.1. Computational procedure

Initially, a linear elastic model of the entire TBC is considered. The reason for carrying out the linear

elastic analysis is that the results of this model enable us to distinguish the nonlinear effect of the elastic–plastic models and isolate the other important physical effects. The elastic–plastic analysis is presented in Section 5. Here, all materials including the NiCrAlY and Ti–6Al–4V are assumed to be linearly elastic and only the elastic properties listed in Table 1 are used. The thicknesses of the ceramic coating and bond coat are chosen as $t_C = 400$ μm and $t_B = 130$ μm, respectively, and represent typical thicknesses of TBCs. The origin of the cylindrical coordinates r and z is shown in Fig. 2(b). Two geometrical locations are considered for an embedded penny-shaped crack. One is a homogeneous crack located somewhere within the ceramic coating and the other is an interface crack lying between the ceramic and bond coats as shown in Fig. 4. Here the depth location is measured from the surface of the ceramic coating and denoted as d. We did not consider cracks at other geometrically significant locations (e.g., within the bond coat) because our previous analysis has shown that the fracture toughness in such locations to be much higher (Qian et al., 1997). The diameter of the penny-shaped crack is assumed to range from $2a = 0.2$ to 8 mm.

In our finite element model, the thickness and radius of the substrate are chosen to be 20 times the thickness of TBCs in order to represent a thick and large substrate. Since a large number of different models must be analyzed, a mesh generator code was developed using 4-node bilinear isoparametric axisymmetric elements. In order to determine the tem-

perature field as well as the deformation field near the crack tip accurately, specially refined elements are placed in the crack tip region. Such a mesh design is also required for accurate calculations of crack tip parameters. Additionally, small elements are used near the boundaries of different layers to capture large strain changes caused by the material mismatch. An axisymmetry condition is prescribed along $r = 0$ while the roller type boundary condition is placed along the bottom of the substrate. No external load is applied in this analysis. About 2000 elements are used in a typical model. To model the crack insulation effect discussed in Section 3.2.2, special interface elements are placed between the crack surfaces. Each interface element is connected to a pair of nodes on the upper and lower faces of the crack. This element permits one-dimensional heat conduction across the 'gap' of an opened crack as determined by the opening displacement between the two nodes based on Eq. (6). Furthermore, these elements prevent the crack faces from overlapping each other when the crack tends to close. Since the heat conduction is a function of the crack opening, the use of these elements make the analysis nonlinear, even for the linear elastic model. Typically, 2 to 3 iterations are carried out to achieve an equilibrium condition at each increment.

4.2. Computational results

Three physical factors can contribute to the growth of internal cracks in the coatings. They are (i) the material mismatch (primarily the CTE difference) among different layers, (ii) the thermal gradients through the coatings, and (iii) the thermal insulation across the crack faces. Here the resulting energy release rate is calculated for different prescribed temperatures using Eq. (2). In addition, the phase angle according to Eq. (4) is determined at every increment from calculated K_I and K_{II}.

In the finite element analysis, the boundary temperatures, both T_{surf} and T_{sub} are initially set at the room temperature (20°C) and increased linearly with time increments but at different rates. The calculations are carried out until $T_{surf} = 1100°C$ and $T_{sub} = 850°C$ are reached. In Fig. 5, the energy release rate is shown as a function of the surface temperature.
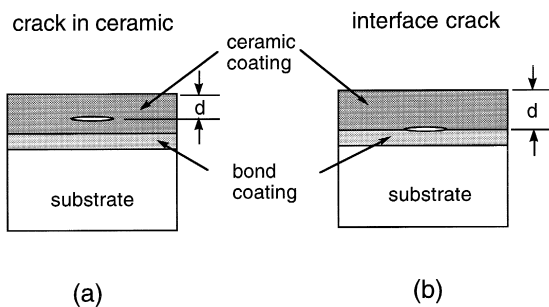

Fig. 4. Two locations of embedded cracks shown in the cross-sections of axisymmetrical models. The location of the crack d is measured from the surface of the ceramic coating. (a) Homogeneous crack within the ceramic coating. (b) Interface crack between the ceramic and bond coatings.
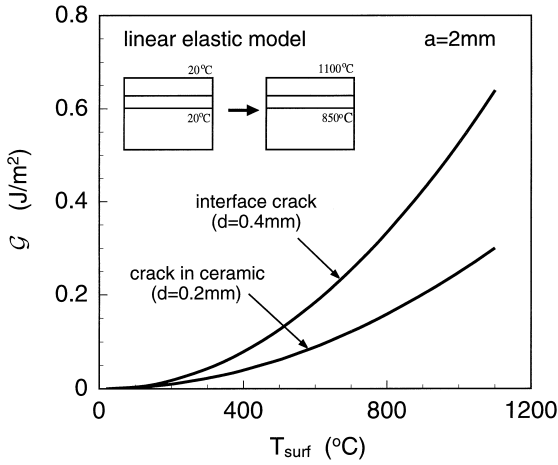
Fig. 5. Energy release rate as a function of the surface temperature. The results are shown for two different crack locations both with $a = 2$ mm. All the materials are assumed as linear elastic.

dominant as revealed by the results of phase angle in Fig. 6(b). Both phase angles decrease for larger crack radii but ψ is always larger for the interface crack because of its geometrical condition. It is interesting to note that the phase angle of the interface crack approaches the steady-state value of about $\psi = 83°$ when the crack radius is greater than $a = 1$ mm while that of the crack within the ceramic persistently decreases as the crack becomes larger. This implies that the faces of the crack in the ceramic tend to open up (i.e., mode I) rather than slide apart (i.e., mode II) when the crack radius increases.
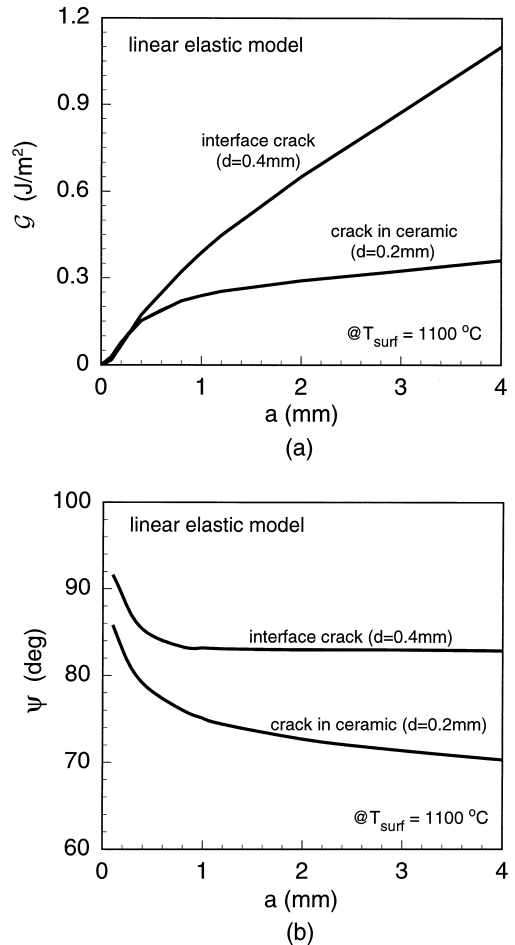
Here, two separate analyses are carried out, one model with the interface crack between the ceramic and bond coats and the other with the homogeneous crack within the ceramic layer at a depth $d = 0.2$ mm. The crack radii of both models are set at $a = 2$ mm. The figure shows $\mathcal{G}$ increasing with temperature. In addition, the energy release rate of the interface crack is about twice that of the crack in the ceramic layer. The interface crack has the higher $\mathcal{G}$ because of the higher shear loading due to the mismatch of materials around the ceramic–bond interface. In fact, the computed phase angles show $\psi = 83°$ for the interface crack while that of the crack in the ceramic is $\psi = 73°$ (note that these values are essentially independent of temperature for the linear elastic model and a phase angle which is closer to 90° implies larger shearing deformation). In fact, K_{II} is greater for the interface crack even though K_I is similar for both cracks during the thermal loading.

We have also investigated the effect of crack radius using various linear elastic models as shown in Fig. 6(a). Here only the results at $T_{surf} = 1100°C$ are shown for both the interface crack and the crack in the ceramic. In general, $\mathcal{G}$ of both cracks increases with the crack radius but at different rates. At small crack radius ($a < 0.3$ mm), the energy release rate of the crack in the ceramic is higher but it is surpassed by that of the interface crack as they grow. In both cases, the crack tip fields are strongly shear-

Fig. 6. The results of linear elastic models at $T_{surf} = 1100°C$ are shown as function of embedded crack radius. (a) Energy release rate. (b) Corresponding phase angle with the characteristic length $L = 2$ μm.

5. Elastic–plastic model

5.1. Computational procedure

Similar thermal boundary conditions and finite element meshes as described in the linear elastic model are employed in elastic–plastic models. Initially the results of temperature-*independent* material models are presented and then the temperature-*dependent* model is used. In this way, the effect of the plastic or nonlinear deformation can be clearly identified by comparison with the elastic results. The properties of the temperature-independent model are listed in Table 1 while those of the temperature-dependent model are listed in Table 2. We note that the temperature-dependent properties are obtained from a collection of limited sources and some data may be approximate. In both cases, the ceramic coating is assumed to remain linear elastic throughout the thermal loading. To ensure the accuracy of the results for the elastic–plastic model, smaller temperature increments are taken. On average, 30 increments are used to raise the surface temperature to 1100°C.

5.2. Results of temperature-independent elastic–plastic model

The results of $\mathscr{G}$ for the 2 mm crack radius are plotted as a function of the surface temperature in Fig. 7(a). For the interface crack, the rise of energy release rate is significantly lower compared with the corresponding $\mathscr{G}$ of the linear elastic model shown in Fig. 5. This result can be attributed to the relaxation of internal stresses due to plastic flow in the metallic bond coat. Physically, as the thermal stress builds up, plastic deformation occurs and leads to reduction in shear loading caused by the material mismatch across the interface. This effect is evident in the phase angle result shown in Fig. 7(b). Here the phase angle of the interface crack is determined from Eq. (5) and plotted as a function of T_{surf}. At a low temperature, the phase angle ψ is close to the result of the linear elastic model ($\psi \simeq 83°$), but as the temperature increases, ψ decreases showing lesser mode II and shear loading.

The energy release rate of the crack in the ceramic at $d = 0.2$ mm is almost identical to that of the
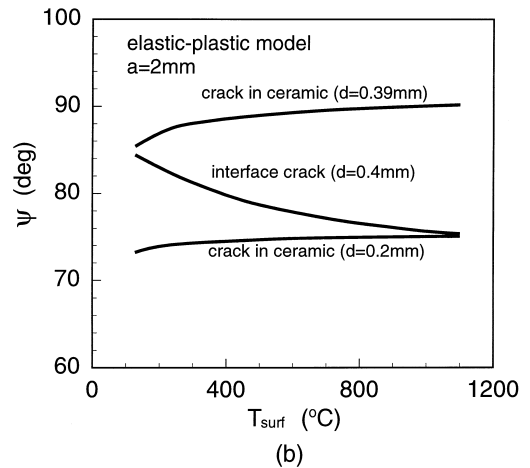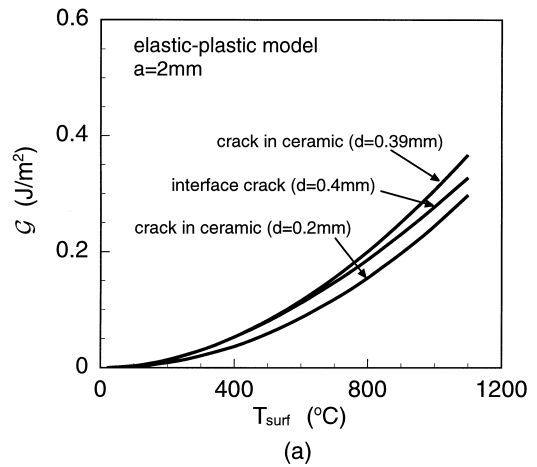

Fig. 7. The results of temperature-independent elastic–plastic models are shown as functions of the surface temperature. There different crack locations are considered. In all cases, the crack radius is $a = 2$ mm. (a) Energy release rate. (b) Corresponding phase angle.

linear elastic model shown in Fig. 5. This result indicates that the plastic flow occurring in the bond coat has a minimum effect on the crack located sufficiently away from the bond coat. Note that the crack depth at $d = 0.2$ mm corresponds to the mid-location of the ceramic layer and the distance of 0.2 mm from the bond coat. A similar result is also observed for the phase angle shown in Fig. 7(b). It shows almost constant ψ during the thermal loading and is essentially equal to the linear elastic result ($\psi \simeq 73°$) This result also confirms that there is little effect of the plastic deformation in the bond coat and

the substrate when a crack is located well within the ceramic coating.

In order to investigate any influence of plastic flow on a crack in the ceramic layer, we have studied another crack located very close to the bond coat. In this model, the crack in the ceramic is placed at $d = 0.39$ mm from the surface, i.e., at a distance of only 10 μm away from the ceramic–bond interface. The energy release rate of this model shows a higher rate of increase with T_{surf} than that of the crack at $d = 2$ mm. These results illustrate the influence of the bond coat plasticity on the near-interface crack. In fact, the energy release rate at $T_{surf} = 1100°C$ of this homogeneous crack is higher than that of the interface crack. Interestingly, the phase angle shown in Fig. 7(b) suggests increasing shear loading as the temperature is increased. Based on these results and the fact that the fracture toughness of the ceramic–bond interface is higher than that of the ceramic coating (Oliveira and Bower, 1996; Qian et al., 1997), a homogeneous crack near the interface may be more susceptible to propagation. This issue will be further discussed in Section 5.3.

5.3. Effect of residual stresses

The residual stresses in a bonded ceramic/metal have been studied both analytically and experimentally (Hsueh and Evans, 1985; Koguchi et al., 1994). As discussed earlier, thermal residual stresses can develop during the fabrication process of TBCs. Since plasma sprayed coatings are made by building up many molten splats, predicting accurate residual stresses is extremely difficult. In fact, any change in the manufacturing process (e.g., flow behavior of splats) can influence the residual stress state within coatings. To circumvent the complexity of modeling the precise cooling down process, we considered a condition which yields extreme residual stresses. It was discussed in Section 3.3 that secondary cooling can be the major factor for large residual stresses in the TBCs. Here, to model the secondary cooling, it is assumed that the whole TBC system is initially at a uniform temperature of 700°C and slowly cooled down to room temperature (20°C). This process results in residual stresses within TBCs due to the CTE mismatch. In such a procedure, the initial temperature also corresponds to the so-called 'zero-stress'

temperature. Alternatively, one can choose another zero-stress temperature to control the amount of residual stress that results at room temperature. Although the choice of 700°C is made arbitrarily, we believe it represents an upper bound of zero-stress temperature of actual TBCs. Thus, cooling down from this temperature should generate close to the maximum residual stress for any TBC. Accordingly, if the actual zero-stress temperature is less than 700°C, then the effect of residual stresses on the fracture parameters should fall between the results of this 700°C model and the model without residual stresses presented in the previous section. The zero-stress temperature of the previous section can be regarded as room temperature (20°C).

Before carrying out the fracture analysis with incorporation of the residual stresses, the state of internal stresses after the cool-down is investigated. The radial residual stress profile is shown in Fig. 8. For our combination of materials, it is found that the stress in the ceramic coating is in compression while it is in tension in the bond coat. The large magnitude of the stress within the bond coat arises from both the given CTE values (shown in Table 1) and its geometrical constraint (i.e, a thin layer bounded between thicker layers). Other characterizations regarding the state of the residual stresses can be also summarized as; (i) residual stresses cause biaxial stress state and the hoop stress σ_θ is the same as the
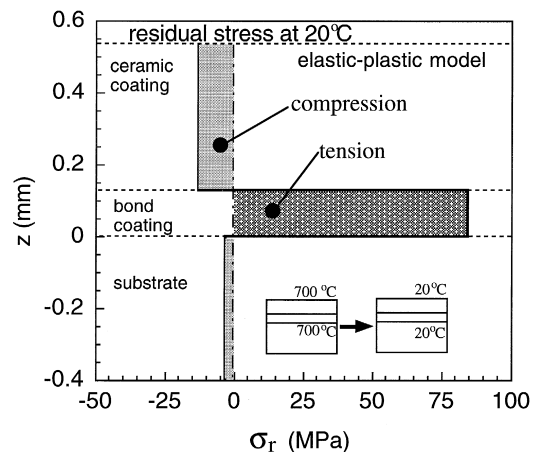

Fig. 8. Profile of radial residual stress through the thickness of elastic–plastic model. The model is uniformly cooled from 700°C to room temperature.

radial stress while the other components of stress are very small, (ii) the residual stress is constant in each layer, and (iii) the compressive stress in the ceramic would discourage crack advance along the vertical direction. We also note that the magnitudes of the residual stresses are very sensitive to the relative values of CTEs.

Although not shown here, the residual stresses of the linear elastic model are also computed. The results show that the radial residual stress reaches close to 480 MPa in the bond coat which is about five times as high as that in the elastic–plastic model. It is clear that yielding in the bond coat reduces the magnitude of residual stresses dramatically. In some earlier papers, the residual stresses in the TBCs were predicted from linear elastic models and these might have exaggerated the magnitudes of the residual stresses. The residual stresses can play an important role in the performance and durability of TBCs (Brindley, 1995) but its effect on the mechanical integrity is yet to be clarified. In order to enhance the quality of TBCs, it is crucial to search for the answer in both qualitative and a quantitative manners. We approached this problem from the perspective of fracture mechanics and results from the elastic–plastic model are presented next.

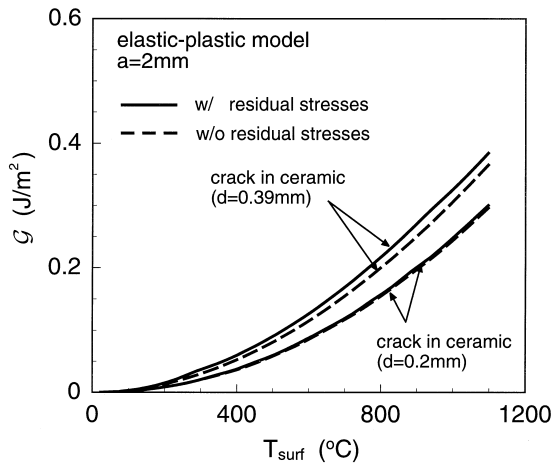In Fig. 9, the energy release rate of crack models

Fig. 9. Energy release rate of elastic–plastic models with residual stresses are shown as functions of the surface temperature. Two different crack locations with in the ceramic locations are considered. The results without residual stresses are also shown for reference.

with residual stresses are shown. First, the TBC model at 700°C is gradually cooled down to room temperature, then it is reheated slowly according to the same process as the one without the residual stresses described in Section 5.2. The calculations are carried out for two homogeneous crack models in the ceramic coating. The interface crack model is not carried out since the large unproportional loading history of the crack tip field within the elastic–plastic bond coat invalidates the existence of J-dominated fields and the use of J (or $\mathscr{G}$) as the fracture parameter. Hence the $\mathscr{G}$ calculated according to Eq. (2) has no physical significance. Note that the loss of dominance does not apply to the cracks in the ceramic coating since they are always within the elastic medium and the elastic K-field can exist near the tip. The result shows that when the crack is located at the mid-location of the ceramic layer ($d = 0.2$ mm), its singular field is essentially insulated from the residual stresses, which implies that compression (observed in Fig. 8) does not influence the energy release rate. However, for the crack located close to the bond coat ($d = 0.39$ mm), the existence of residual stress predicts an increase in the energy release rate. It is about $5 \sim 10\%$ higher than the one without the residual stresses. This result suggests that the large residual tension in the bond coat may have a small detrimental effect on the TBC. It was reported that coating failures often initiate near the interface inside the ceramic coating and bond coat oxidation was proposed to explain such a phenomenon (Bartlett and Maschio, 1995). Based on the current result, residual stresses in coatings may also play a role in such a coating failure and the increased energy release rate due to the residual stresses can affect the TBCs mechanical integrity and its service lifetime.

5.4. Effects of crack location and size in ceramic coating

In the previous two sections, we have observed that the energy release rate changes with the depth location of a crack within the ceramic layer. To investigate this effect further, we have analyzed various cracks at different crack locations. Initially, the crack radii are kept at $a = 2$ mm. In Fig. 10(a), the
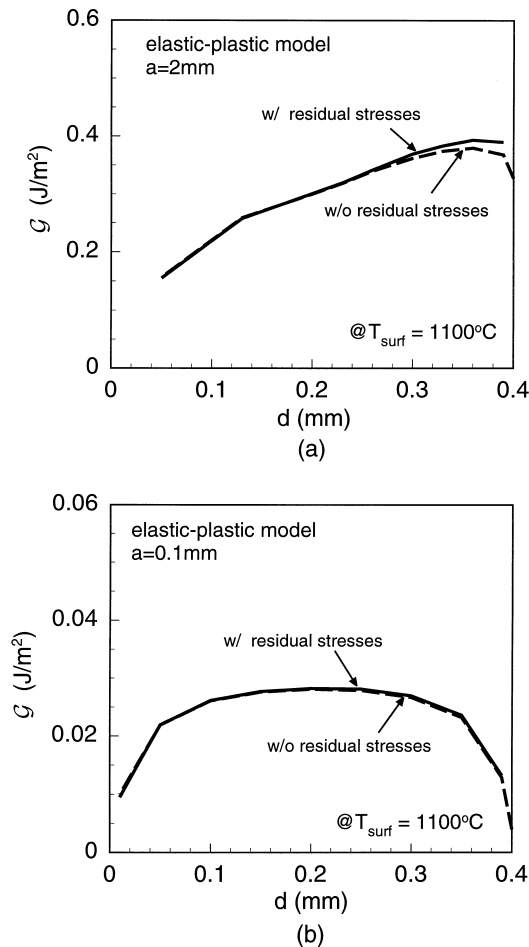
Fig. 10. Energy release rate of elastic–plastic models with and without residual stresses are shown for various crack through the ceramic layer thickness. The surface temperature is $T_{surf} = 1100°C$. (a) For the crack radius $a = 2$ mm. (b) For the crack radius $a = 0.1$ mm.

energy release rate at $T_{surf} = 1100°C$ determined at different crack depths measured from the surface of the ceramic coating (i.e., $d = 0.05$, 0.13, 0.2, 0.23, 0.3, 0.33, 0.36, 0.39 mm) are shown under conditions with and without the residual stresses. The results show that $\mathscr{G}$ of a crack close to the free-surface ($d = 0.05$ mm) is low and it increases for cracks deeper within the ceramic coating. In the figure, the maximum $\mathscr{G}$ occurs near $d = 0.36$ mm with or without residual stresses. The implication of these results is that a crack located near the bond coat interface is more likely to propagate.

Since many initial voids and micro-cracks are much smaller in size, we have carried out similar analyses for penny-shaped cracks with a small radius. The energy release rate calculated from cracks with $a = 0.1$ mm at $T_{surf} = 1100°C$ is shown in Fig. 10(b). The magnitude of $\mathscr{G}$ is about an order smaller than $\mathscr{G}$ of the larger crack ($a = 2$ mm), which is consistent with the elastic results shown in Fig. 5(a). The variation of $\mathscr{G}$ through the depth is quite different from the larger crack results. The maximum $\mathscr{G}$ occurs near the middle section of the ceramic coating and the residual stresses have virtually no effect on these small cracks. We have also tested a crack of intermediate radius ($a = 0.5$ mm) and found that its $\mathscr{G}$ falls between the results of the large ($a = 2$ mm) and the small ($a = 0.1$ mm) cracks.

5.5. Effects of crack orientation

In order to gauge the effect of residual stresses further, we have modeled a crack which is perpendicular to the coating layers. Since an axisymmetry does not exist for such a crack, we have assumed the plane strain condition. Note this crack model is only used and presented in this section.

From the investigation of radial stress through thickness, we have found that the entire ceramic coating generally stays in compression throughout the thermal loading. This implies that any cracks which are perpendicular to the coating layers remain closed and do not grow. However, there is an isolated region very near the bond coat where the radial stress becomes tensile as the prescribed temperature increases. In order to quantify the effect of residual stresses on possible crack growth, a small perpendicular crack whose length is $a = 25$ μm is embedded within the ceramic coating as shown in the inset of Fig. 11. The bottom tip of this crack is only 10 μm away from the interface of the ceramic and bond coats while the top tip is 365 μm away from the surface of ceramic coating. The energy release rate of this crack is calculated with and without residual stresses and shown in Fig. 11. Aside from the crack orientations, the material model and loading procedure are the same as the ones described for the penny-shaped crack. Note that each crack contains two tips and the energy release rate is shown for both cases. Without residual stresses, both tips open
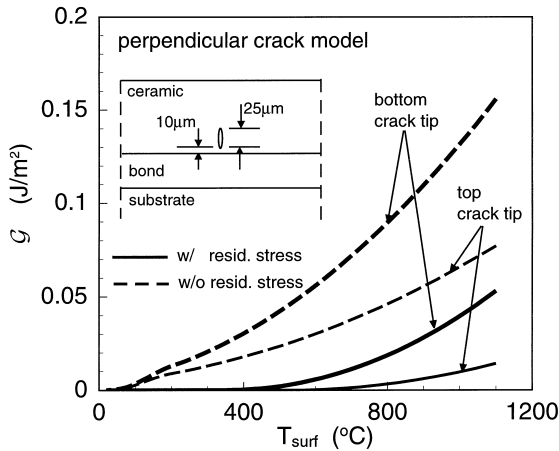
Fig. 11. Energy release rate of a plane strain perpendicular crack with and without residual stresses are shown as functions of the surface temperature. The top and bottom crack tips correspond to the two crack tips of a single crack.

up and the energy release rate increases with the surface temperature. With residual stresses, the crack tips initially remain closed due to the compressive residual stress in the ceramic layer as seen in Fig. 8.

As the temperature increases and sufficient tension builds up near the interface, the bottom tip opens up at around $T_{surf} = 400°C$ and the top tip opens up at around $T_{surf} = 600°C$ as indicated by the $\mathscr{G}$ increase in Fig. 11. However, with residual stresses, the final energy release rate is significantly lower than that of the crack without residual stresses. This result suggests that the residual stresses have a beneficial effect in preventing crack growth. Although not shown here, the magnitude of energy release rate is higher for cracks located even closer to the bond coat.

5.6. Results of temperature-dependent elastic–plastic model

Since many material properties of coatings are actually temperature-dependent, an elastic–plastic model with temperature-dependent elastic moduli, yielding stresses and CTEs is studied here. Only the penny-shaped cracks parallel to the coating layers are considered. For the material model, the properties listed in Table 2 are used. Three different locations of cracks, i.e., an interfacial crack ($d = 0.4$

mm), a crack at mid-section of the ceramic ($d = 0.2$ mm) and a crack in the ceramic but close to the interface ($d = 0.39$ mm), are investigated. The crack radius is set at $a = 2$ mm for all cases. Models with residual stresses are also analyzed for the latter two cases. The ceramic itself is still modeled as a linearly elastic temperature-independent material. The computed energy release rates and phase angles are shown as functions of the surface temperature in Fig. 12(a) and (b), respectively.

The overall characteristics of the results can be observed as follows. For the mid-section crack in the
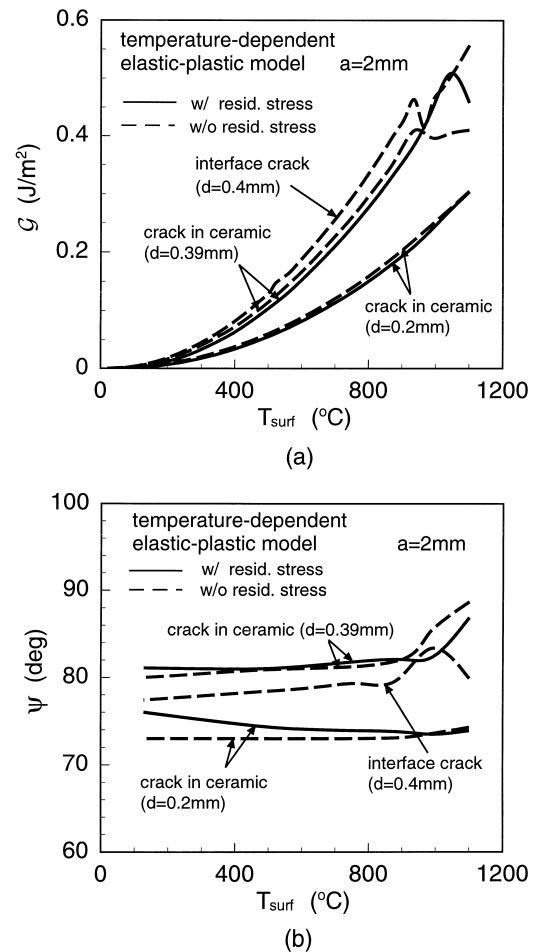

(a)

(b)

Fig. 12. The results of temperature-dependent elastic–plastic models with and without residual stresses are shown as functions of the surface temperature. Three different crack locations are considered. (a) Energy release rate. (b) Corresponding phase angle.

ceramic coating ($d = 0.2$ mm), the energy release rate is almost the same as that of the temperature-independent elastic–plastic model as well as the linear elastic model. The model with residual stresses also shows near identical results. As described earlier, the bond coat plasticity has a very limited effect on a ceramic crack if it is sufficiently away from the ceramic–bond interface. Its phase angle shown in Fig. 12(b) is also very similar to ψ shown in Fig. 7(b)

For the ceramic–bond interfacial crack at $d = 0.4$ mm, the energy release rate is significantly larger than that of the temperature-independent elastic–plastic model (Fig. 7(a)). This $\mathscr{G}$ almost coincides with that of the linear elastic case (Fig. 5) when the surface temperature is below 900°C. The reason is that the yielding within the bond coat and substrate is very limited before the surface temperature reaches 900°C or the temperature in the coating is less than about 650°C. As seen in Table 2, a dramatic drop occurs in the yield stress of NiCrAlY between 650°C and 700°C (note that the yield stress of the temperature-independent model is based on the value at 900°C, which is very low). Thus, the deformation mechanism is very close to that of the linear elastic model for $T_{\mathrm{surf}} < 900$°C. Once T_{surf} exceeds 900°C, $\mathscr{G}$ suddenly dips as the temperature increases. The dip in the energy release rate is attributed to the rapid decrease of the bond coat yield stress which initiates softening of the bond coat through large plastic flow. As the surface temperature continues to climb, the energy release rate rises again. The phase angle of the interface crack also shows a sudden increase and then decrease near $T_{\mathrm{surf}} = 900$°C.

A similar result is observed for the ceramic crack near the interface at $d = 0.39$ mm. Its energy release rate increases with T_{surf} but stabilizes near $T_{\mathrm{surf}} = 900$°C. For the model with the residual stresses, the decrease occurs at a higher temperature since the (current) yield stress at a given temperature is raised by previous plastic flow during the cool-down. The more significant result of this crack is that its energy release rate is much higher than that of the crack at mid-location ($d = 0.2$ mm). These results suggest that propagation is more likely to occur for cracks located closer to the ceramic–bond interface. The phase angle of this crack shows an increasing mode II contribution as the temperature increases.

6. FGM model

6.1. Computational model

The functionally graded materials (FGMs) have drawn more attention in recent years. The concept of a FGM is to combine different materials during a well-controlled process such that the desired variations of material properties are obtained for the newly-obtained FGM. By tailoring the multilayered coating structure to create the variant compositions and/or microstructures in certain coating directions, the designers hope to achieve a higher coating toughness and reduce the peak stress level in the TBC (Lee et al., 1996). Although the full benefits of the FGMs used in the TBCs are yet to be fully understood, the FGM concept may be proven as a viable method to optimize TBCs for certain applications.

When the FGM is used in TBCs, the desired variations of properties are often in the coating thickness direction. In this paper, it is assumed that a FGM layer is sandwiched between the ceramic and bond coatings. The FGM is 100% YSZ at the FGM–ceramic interface and 100% NiCrAlY at the FGM–bond interface. Between these two interfaces, its composition varies linearly through its thickness. It is assumed that the FGM thickness is 100 μm in the computational model.

There have been many efforts to model FGMs. For example, the FGM can be modeled as a multi-layered heterogeneous material but in each layer, the material is homogeneous (Delale and Erdogan, 1988). In this paper, the above approach is adopted in our finite element procedure. Specifically, a total of 20 element layers with the same thickness are used and the thickness of each layer is 5 μm. All material properties remain unchanged in each layer but vary from layer to layer. Therefore, the variations of the material properties in the FGM model are actually discreet in the thickness direction. In fact, the thickness of a splat which is the basic forming unit of the coatings is about 1 μm to 5 μm and the material properties are invariant in a single splat.

It is assumed that the elastic modulus, CTE and thermal conductivity are variant linearly in the thickness direction inside the FGM. Note that linearity here indicates that the material properties at the center of each layer can be correlated by some linear

curves since the actual variations discussed above are discreet due to the finite thickness of each individual layer. If two materials sandwiching the FGM are linear elastic materials, the above assumption in the computational model will suffice. In the elastic–plastic model, the elastic–plastic bond coat material is mixed with the elastic ceramic to produce the FGM. Now the question arises on how to model the FGM yielding since the ceramic which forms part of the FGM does not yield. There have been many efforts to use a matrix-inclusion model based on the Mori–Tanaka method to model the ceramic/metal mixture and, hence, the FGM (Weissenbek et al., 1997). In this paper, a simpler mixture rule of FGM yielding model is proposed for the yielding of the FGM composed of a variant ceramic/metal mixture.

We assume that the FGM also behaves like a linear hardening material but its yielding stress σ_0 and tangent modulus H vary at different FGM thickness. In addition, the tangent modulus H varies linearly from the tangent modulus of the bond coat $H = 5$ GPa at the FGM-bond interface to the elastic modulus of the ceramic coating $E = 30$ GPa at the FGM–ceramic interface. For defining initial yield stress, the following steps are taken. Imagine the yield point of the bond coat as shown in Fig. 13. The initial stress-strain response of a specific ceramic–

metal (i.e., cermet) composition is interpolated by proportioning the mechanical property contributions from each component. In an alike fashion, the final stress-strain response of the cermet as it hardens after yielding can also be calculated. The yield stress of a particular FGM composition at a given z in the figure can then be found by the intersection of the elastic stress-strain and the hardening curves that have been calculated. The computed linear hardening curves at a few selected FGM thicknesses are shown in Fig. 13. It is clear that the FGM behaves more and more linearly elastically as it approaches the ceramic coating over its total thickness of 100 μm. Although the operational definition we adopted may be an oversimplification of the actual FGM coating, the results of this model should still prevail the qualitative trend of the FGM model.

6.2. Results

The energy release rate of a crack in the elastic–plastic FGM layer is calculated. The ceramic and bond coating materials which sandwich the FGM are still YSZ and NiCrAlY respectively. The total thickness of the TBC remains the same at 530 μm but the thicknesses of the ceramic and bond coatings are reduced to $t_C = 350$ μm and $t_B = 80$ μm to accommodate $t_{FGM} = 100$ μm. A penny-shaped crack of radius $a = 2$ mm is assumed to be located in the middle of the FGM, namely, the crack depth which is measured from the top surface of the TBCs is $d = 0.4$ mm. This is the identical depth as the interface crack in the distinct layers shown before.

Only the 'no residual stress case' is considered. The curve of the energy release rate versus the surface temperature is shown for the FGM crack in Fig. 14. For comparison, $\mathscr{G}$ corresponding to the interface crack of the elastic–plastic model (Fig. 7(a)) located at the same depth ($d = 0.4$ mm) is also shown in the figure. It is clear that the increase of the energy release rate accelerates as the surface temperature goes up. The energy release rate from an FGM crack is significantly larger than that of the interface crack. The FGM eliminates a distinct interface between the ceramic and bond coatings so that the stress concentrations near the crack should be reduced. But the FGM model has effectively increased
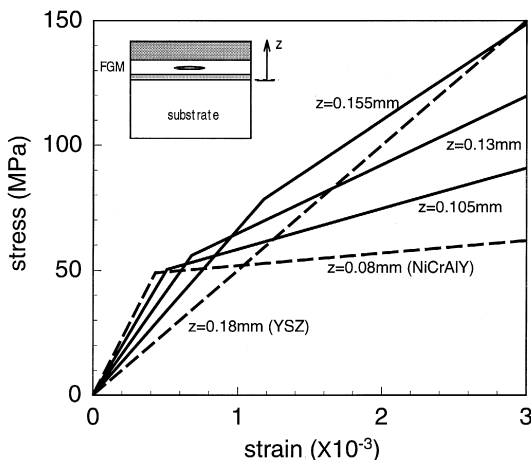

Fig. 13. Stress-strain relations of functionally graded materials bounded by ceramic and bond coats within 0.105 mm $< z <$ 0.18 mm. Dashed lines are the stress-strain of pure elastic ceramic (YSZ) and elastic–plastic bond material (NiCrAlY).
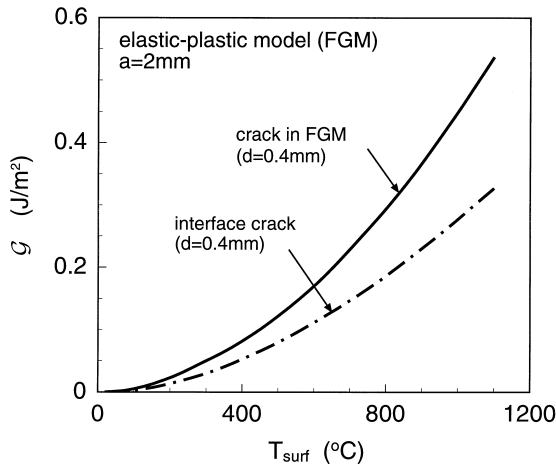
Fig. 14. Energy release rate of FGM model without residual stresses is shown as function of the surface temperature. For a reference, the results of the interface crack of the temperature-independent elastic–plastic model is shown. Both models have the same depth locations measured from the surface of the ceramic coating.

the yield stress and, thus its $\mathcal{G}$ is quite similar to the $\mathcal{G}$ of the linear elastic crack shown in Fig. 5.

7. Conclusions

Fracture behavior of a penny-shaped crack inside TBCs parallel to the coating layers is studied using axisymmetrical formulations. Main factors which are included in the analysis is the thermal gradient within the coating and the residual stresses. In addition, an embedded crack which is perpendicular to the coating layer is also investigated for understanding how fracture energy is influenced by the crack orientation. The substrate is treated as very thick compared with the coatings so that the effect of substrate thickness is ignored. Furthermore, many results are presented for larger crack models where the coating thickness is the only characteristic length scale.

We have constructed and analyzed a large number of models, but only the results which are more physically important are presented here. Although idealization is made for both the material property and the geometrical condition of TBCs, the present results reveal important mechanical features and they are summarized below.

(i) Our overall results indicate that the thermal gradient through the coating plays an important role in understanding the crack driving mechanisms in TBCs. Indeed, many aspects of fracture are different from models where a constant temperature is imposed in the coating. In general, for penny-shaped cracks oriented parallel to the coating layers, the near crack tip field is found to be shear-dominant and the mode I stress intensity factor contributes little to the total energy release rate.

(ii) Based on the results of the elastic–plastic model, we have found that plasticity in the bond coat can be a major factor in the fracture behavior of the coatings. The plastic deformation in the bond coat releases constraint caused by the material mismatch and reduces the internal stresses of the TBCs. In the case of a ceramic–bond interfacial crack, the magnitude of the energy release rate is reduced significantly with a large plastic flow in the bond coat. For the ceramic coating, this effect is confined to cracks located close to the ceramic–bond interface. In this sense, the ductile bond coat is beneficial to the integrity of TBCs as long as the large deformation does not lead to the bond coat failure.

(iii) Secondary cooling, imposed during TBC manufacture, is examined as the most conspicuous mechanism which generates residual stresses in TBCs. The residual stresses based on the elastic–plastic model are shown to be small for cracks parallel to the coating layers. A much greater effect is observed for the cracks perpendicular to the coating layers where the compressive residual stress lowers the energy release rate at the high temperature. However, in the ceramic coating, cracks open up or tend to propagate only if they are very close the ceramic–bond interface.

(iv) We have also studied the likely location of crack propagation for the cracks parallel the coating layers in the ceramic. It was found that the energy release rate is largest at the mid-section of the coating for a small crack while it has the maximum value near the ceramic–bond interface for a long crack. This result can explain why many coating failures are observed near the interface but inside the ceramic coating.

(v) The temperature-dependent models give rise to more complex results concerning the crack tip parameters. It appears that a drastic change can occur

when the temperature of the bond coat reaches the temperature when the Young's modulus and the yield stress of the bond material suddenly drop. In general, the energy release rate of the temperature-dependent model is higher than that of the temperature-independent model under similar loading conditions. In addition, the effect of residual stresses is magnified with this model.

(vi) A simplified yielding model is used for a FGM which is sandwiched between the elastic ceramic layer and the elastic–plastic bond layer. Results concerning a penny-shaped crack embedded at the center of the FGM show that a FGM crack actually increases the magnitude of the energy release rate as compared to a similarly placed interface crack. Although the FGM may not be beneficial from the mechanical point of view, it eliminates the distinct interface and may provide a stronger bonding between the ceramic layer and the bond layer.

On the basis of this work, optimally controlling the residual stresses can be regarded as one possibility for reducing internal cracking of TBCs. Furthermore, other materials can be used for the bond coat to lower tensile stress within the ceramic coating during the thermal loading.

Acknowledgements

References

Bartlett, A.H., Maschio, R.D., 1995. Failure mechanisms of a zirconia–8 wt% yttria thermal barrier coating. J. Am. Ceram. Soc. 78, 1018.

Bengtsson, P., Johannesson, T., 1995. Characterization of microstructural defects in plasmasprayed thermal barrier coatings. J. Therm. Spray Tech. 4, 245.

Bever, M.B. (Ed.), 1986. Encyclopedia of Materials Science and Engineering 7. Pergamon and MIT Press, p. 5543.

Brandes, E.A., et al. (Ed.), 1992. Smithells Metal Reference Book, 7th ed. Butterworth Heinemann Ltd.

Brandon, J.R., Taylor, R., 1989. Thermal properties of ceria and yttria partially stabilized zirconia thermal barrier coatings. Surf. Coat. Tech. 39/40, 143.

Brindley, W.J., 1995. Properties of plasma sprayed bond coat. NASA Conference Pub. SS12. Cleveland, OH, p. 235.

Cao, H.C., Evans, A.G., 1989. An experimental study of the fracture resistance of bimaterial interfaces. Mech. Mater. 7, 295.

Cook, L.S., Wolfenden, A., Brindley, W.J., 1994. Temperature dependence of dynamic Young's modulus and internal friction in LPPS NiCrAlY. J. Mater. Sci. 29, 5104.

Delale, F., Erdogan, F., 1988. On the mechanical modeling of the interfacial region in bonded half-planes. J. Appl. Mech. 55, 317.

Elsing, R., Knotek, O., Balting, U., 1990. The influence of physical properties and spraying parameters on the creation of residual thermal stresses during the spraying process. Surf. Coat. Tech. 43/44, 416.

Eckert, E.R.G., Drake, R.M., Jr., 1972. Analysis of Heat and Mass Transfer. McGraw-Hill, New York.

Harding, J.H., Mulheran, P.A., Cirolini, S., Marchese, M., Jacucci, G., 1995. Modeling the deposition process of thermal barrier coating. J. Therm. Spray Tech. 4, 34.

Herman, H., Shankar, N.R., 1987. Survivability of thermal barrier coatings. Mater. Sci. Eng. 88, 69.

Hobbs, M.K., Reiter, H., 1988. Residual stresses in ZrO_2–8%Y_2O_3 plasma-sprayed thermal barrier coatings. Sur. Coat. Tech. 34, 33.

Hsueh, C.H., Evans, A.G., 1985. Residual stresses in metal/ceramic bonded strips. J. Am. Ceram. Soc. 68, 241.

Hutchinson, J.W., Lu, T.J., 1995. Laminate delamination due to thermal gradients. J. Eng. Mater. Tech. 117, 386.

Illavsky, J., Berndt, C.C., Herman, H., Beardsley, M.B., 1993. Thermal expansion of metallic and cermet coatings. In: Proc. 1993 Nat. Therm. Spray Confer., Anaheim, CA, p. 601.

Koguchi, H., Hino, T., Kikuchi, Y., Yada, T., 1994. Residual stress analysis of joints of ceramics and metals. Exper. Mech. 34, 116.

Kokini, K., Choules, B.D., Takeuchi, Y.R., 1997. Thermal fracture mechanisms in ceramic thermal barrier coatings. J. Therm. Spray Tech. 6, 43.

Lee, E.Y., Biederman, R.R., Sisson, R.D., 1989. Diffusional interactions and reactions between a partially stabilized zirconia thermal barrier coating and the NiCrAlY bond coat. Mat. Sci. Eng. A 120, 467.

Lee, W.Y., Stinton, D.P., Berndt, C.C., Erdogan, F., Lee, Y.D., Mutasim, Z., 1996. Concept of functionally graded materials for advanced thermal barrier coating applications. J. Am. Ceram. Soc. 79, 3003.

Leigh, S.H., 1996. Stereological investigation on structure/property relationships of plasma spray deposit. Ph.D. thesis, State University of New York at Stony Brook, USA.

Liebert, C.H., Miller, R.A., 1984. Ceramic thermal barrier coatings. Ind. Eng. Chem. Prod. Res. Dev. 23, 344.

McPherson, R., 1989. A review of microstructure and properties of plasma sprayed ceramic coatings. Surf. Coat. Tech. 39/40, 173.

Miller, R.A., 1997. Thermal barrier coatings for aircraft engines: History and directions. J. Therm. Spray Tech. 6, 35.

Nahta, R., Moran, B., 1993. Domain integrals for axisymmetric interface crack problems. Int. J. Solids Struct. 30, 2027.

Oliveira, S.A.G., Bower, A.F., 1996. Analysis of fracture and delamination in thin coatings subjected to contact loading. Wear 198 (1–2), 15.

Qian, G., Nakamura, T., Berndt, C.C., Leigh, S.H., 1997. Tensile fracture test and high temperature fracture analysis of thermal barrier coatings. Acta Mater. 45, 1767.

Shih, C.F., Moran, B., Nakamura, T., 1986. Energy release rate along a three-dimensional crack front in a thermally stressed body. Int. J. Frac. 30, 79.

Siemers, P.A., Melan, R.L., 1983. Mechanical and physical properties of plasma-sprayed stabilized zirconia. Ceram. Eng. Sci. Proc. 4, 828.

Takeuchi, S., Ito, M., Takeda, K., 1990. Modeling of residual stress in plasma-sprayed coatings: Effect of substrate temperature. Surf. Coat. Tech. 43/44, 426.

Touloukian, Y.S., 1970. In: Y.S. Touloukian et al. (Ed.), Thermophysical Properties of Matter–Thermal Conductivity, 1–2. IFI/Plenum, New York–Washington.

Weissenbek, E., Pettermann, H.E., Suresh, S., 1997. Elasto–plastic deformation of compositionally graded metal–ceramic composites. In press.